Retrosplenial inputs drive visual representations in the medial entorhinal cortex

Olivier Dubanet[1], **Michael J. Higley**[1,2,*]

[1]Department of Neuroscience, Kavli Institute for Neuroscience, Wu Tsai Institute, Yale University, New Haven, CT 06510, USA

[2]Lead contact

SUMMARY

The importance of visual cues for navigation and goal-directed behavior is well established, although the neural mechanisms supporting sensory representations in navigational circuits are largely unknown. Navigation is fundamentally dependent on the medial entorhinal cortex (MEC), which receives direct projections from neocortical visual areas, including the retrosplenial cortex (RSC). Here, we perform high-density recordings of MEC neurons in awake, head-fixed mice presented with simple visual stimuli and assess the dynamics of sensory-evoked activity. We find that a large fraction of neurons exhibit robust responses to visual input. Visually responsive cells are located primarily in layer 3 of the dorsal MEC and can be separated into sub-groups based on functional and molecular properties. Furthermore, optogenetic suppression of RSC afferents within the MEC strongly reduces visual responses. Overall, our results demonstrate that the MEC can encode simple visual cues in the environment that may contribute to neural representations of location necessary for accurate navigation.

Graphical Abstract
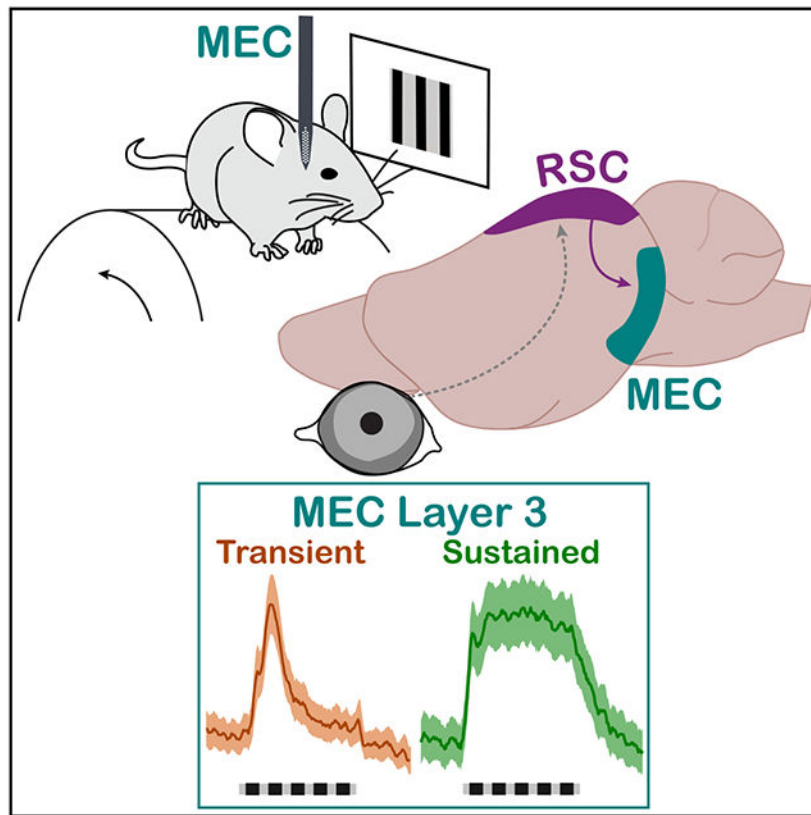
In brief

Dubanet and Higley show that single neurons in the mouse medial entorhinal cortex show robust, time-locked responses to simple visual stimuli. Visually driven cells are located primarily in layer 3 and exhibit distinct response dynamics and expression of molecular markers. Optogenetic suppression of retrosplenial inputs strongly inhibits visually evoked activity.

INTRODUCTION

Spatial navigation requires coordinated activity within the hippocampus and closely connected entorhinal cortex.[1,2] However, navigation also requires the integration of sensory cues and internally generated motor signals.[3] The combination of these various streams of information are thought to give rise to canonical patterns of spiking that correspond to environmental locations and features. For example, grid cells in the medial entorhinal cortex (MEC) fire at vertices of a lattice spanning the local environment,[4] and place cells in the hippocampal CA1 subregion exhibit activity that maps onto specific places.[5] Additionally, MEC neurons are also responsive to behavioral and environmental features, including borders, task-relevant timing, and speed of locomotion,[6–10] and there is growing appreciation that sensory cues can influence MEC activity.[11,12]

The ability of rodents to use visual cues for successful navigation and goal-directed behavior has long been appreciated.[5,11–14] Visual information can anchor place and grid cells during navigation,[4,15,16] and loss of visual inputs or decoupling of the relationship between visual

flow and self-motion can disrupt the activity of hippocampal and MEC neurons.[10,12,15] Moreover, "cue" cells in the MEC exhibit repeatable firing fields near salient visual features.[11,12] Computational work suggests the importance of visual information as a mechanism for error correction during path integration.[17–19] In recent work, investigators used virtual reality tasks in which the rodent navigates an environment consisting only of visual cues, finding normal emergence of grid cell dynamics.[11,20,21] One possibility is that neurons in the MEC inherit complex visual representations from upstream areas like the retrosplenial cortex (RSC), a neocortical area that also encodes relational properties of visual landmarks and environment boundaries.[22–24] Alternatively, the MEC may directly encode simple, low-dimensional visual information, allowing local entorhinal and hippocampal circuits to integrate such cues with more complex behaviorally relevant signals.

Traditionally, multimodal and highly processed unimodal sensory inputs arising from the neocortex are thought to target superficial layers in the MEC, whose cells relay those signals to the hippocampus.[25–28] However, neurons in occipital neocortical regions, including primary and secondary visual areas as well as the RSC, also innervate layer 5,[26,27,29] and optogenetic activation of RSC fibers in the MEC *ex vivo* can evoke excitatory postsynaptic potentials in layer 5 neurons.[29] Additionally, MEC cells comprise distinct subpopulations defined not only by laminar position but by molecular markers, including reelin, calbindin, and Ctip2.[25] Despite these findings, the identity of visually responsive cells in the MEC and their sensitivity to specific visual stimulus features remain unknown.

Here, we performed high-density recordings of MEC neurons in awake, head-fixed mice presented with simple visual stimuli and assessed the dynamics of sensory-evoked activity. Our results demonstrate that ~40% of MEC neurons exhibit robust, time-locked activity in response to visual inputs. Notably, most visually responsive cells appear to be located in layer 3, where they exhibit variation in molecular markers and functional response profiles. Moreover, visual inputs strengthen the coupling of MEC output to ongoing network dynamics, suggesting a role for shaping circuit activity linked to behavior. Finally, we find that suppressing retrosplenial inputs to the MEC significantly disrupts visually driven activity, suggesting that this pathway is a key mediator of visual representations in the hippocampal formation.

RESULTS

MEC neurons are responsive to simple visual stimuli

To study sensory-evoked neural dynamics in the MEC, we recorded single-unit and local field potential (LFP) activity in head-fixed, freely running mice presented with small patches of contrast-modulated drifting gratings (1-s stimuli, 4-s interstimulus interval, 100% contrast, 0.04-Hz spatial frequency, 2-Hz temporal frequency, 100° size, vertical orientation, presented to the center of the visual field; Figure 1A). Neuronal output was sensitive to changes in behavioral state, estimated by fluctuations in locomotion and pupil diameter as well as onset of visual cues (Figure 1B). Indeed, we found that a surprisingly large fraction of MEC neurons was highly modulated by visual input (Figures 1C–1E; STAR Methods). Most responsive cells (38% of all neurons) exhibited increased firing rates during the stimulus presentation, while a smaller proportion (4%) was suppressed (Figure 1D).

We next investigated the potential for single neurons to represent specific properties of the visual stimuli in their signal-to-noise ratio (SNR), defined as the evoked response normalized by the baseline firing rate. We found that, across animals, evoked activity increased with stimulus contrast (Figure 1E). Additionally, MEC visual responses were monotonically enhanced by increasing stimulus size but were largely unaffected by varying its spatial frequency or orientation (Figure S1). Responses were also similar for both drifting and static (inverting) gratings but were somewhat greater for stimuli presented solely to the contralateral versus ipsilateral eye (Figure S1). Finally, we did not detect a bias in sensitivity for stimuli presented at different locations across the visual field (Figure S1). Overall, these results are consistent with a view of the MEC as a hierarchically upper-level visual area with high sensitivity and large receptive fields but low specificity for simple sensory cues.

Laminar and molecular identity of visually responsive MEC neurons

The MEC comprises a highly diverse population of neurons that vary as a function of both cortical layer and position along the dorsal-ventral axis.[25] Therefore, we next sought to characterize the identity of MEC neurons responsive to visual inputs. First, we examined the presence and magnitude of visual responses as a function of recording location (determined by DiI labeling of the electrode). A greater percentage of cells were responsive and exhibited a significantly larger SNR for the dorsal versus ventral half of the MEC (dorsal SNR = 0.97 $\pm$ 0.79 vs. ventral SNR 0.28 $\pm$ 0.17, $p = 0.011$, linear mixed effects model [LMEM], dorsal responsive cells 62.1% $\pm$ 13.7% vs. ventral responsive cells 8.5% $\pm$ 3.27%, $p = 0.0013$, LMEM, $n = 67$ total dorsal cells and 90 total ventral cells in 3 mice; Figure 2A).

We confirmed this finding using FosTRAP transgenic mice that allow fluorescent tdTomato labeling of active neurons within a brief temporal window.[30] After 5 days in dark housing, mice were injected with hydroxytamoxifen and presented with visual stimuli for 30 min. After 1 week, mice were perfused, and tdTomato expression was quantified within the MEC. As expected from our recordings, red fluorescent cells were located primarily in the dorsal MEC. In addition, all MEC layers exhibited a significant increase in labeled cells following visual stimulation in comparison to non-stimulated control animals (layer 1: 0.52 $\pm$ 0.36 vs. 0 $\pm$ 0 converted cells/100 μm^2, $p = 0.0016$; layer 2: 1.5 $\pm$ 0.74 converted cells/100 μm^2 vs. 0.13 $\pm$ 0.09 converted cells/100 μm^2, $p = 9.9e–4$; layer 3: 4.73 $\pm$ 0.74 converted cells/100 μm^2 vs. 0.25 $\pm$ 0.08 converted cells/100 μm^2, $p = 6.52e–5$; layer 5: 2.25 $\pm$ 0.89 converted cells/100 μm^2 vs. 0.25 $\pm$ 0.15 converted cells/100 μm^2, $p = 8.53e–5$; $n = 6$ visual stimulation vs. 3 control mice; LMEM with Bonferroni correction; Figure 2B). However, the greatest density of cells was labeled in layer 3 (layer 1 vs. layer 3, $p = 1.13e–8$; layer 2 vs. layer 3, $p = 6.35e–7$; layer 5 vs. layer 3, $p = 1.82e–5$; LMEM with Bonferroni correction; Figure 2B).

To further investigate the molecular identity of visually responsive neurons, we used an adeno-associated viral (AAV) vector to express the activity-dependent fluorescent marker CaMPARI2 in the MEC and delivered ultraviolet (405 nm) light to the MEC during presentation of visual stimuli identical to our recording experiments.[31] Our results showed that CaMPARI2 expression was primarily found in layer 3 of the MEC (Figure 2C). Moreover, approximately 48% of cells were photoconverted by delivery of visual stimulation (Figure 2D), similar to the proportion of visually responsive neurons

by recording. Omission of visual stimulation resulted in only ~3% of cells being photoconverted, suggesting that red labeling is specific to visually responsive neurons (47.78% ± 20.52% stimulated vs. 3.42% ± 2.05% control, $p = 0.0158$, LMEM, $n = 9$ stimulated and 2 control mice; Figure 2D). To determine the molecular signatures of visually responsive cells, we immuno-stained CaMPARI2-labeled tissue for markers of known MEC subtypes, including calbindin, reelin, and Ctip2. Of these, less than 10% of photoconverted cells were positive for either calretinin or reelin, but ~25% were positive for Ctip2 ($n = 3$ mice per marker; Figures 2D and S2). Together, these results suggest that visually responsive neurons in the MEC comprise a molecular diverse population concentrated in layer 3.

Heterogeneous visual response properties in the MEC

We observed substantial heterogeneity in the temporal profile of visual response across the population of MEC neurons. Many cells exhibited a transiently higher output at stimulus onset that decayed rapidly to a sustained elevated rate (Figure 1C), a finding that might arise from either a distinct pattern of input from upstream visual areas or differential local connectivity shaping the response to afferent drive. We quantified this tendency for single cells by calculating an adaptation ratio of firing during the late versus early phase of the response (Figures 3A and S3). Cells in the lower and upper quartiles were defined as transient and sustained, respectively, and investigated further to explore population differences in response dynamics (Figure 3B). These two categories were observed simultaneously within a recording session and did not differ in spike waveform characteristics either from each other or from visually non-responsive cells (Figure S3). Sustained and transient cells exhibited similar spontaneous firing rates that were larger than those of non-responsive cells (2.96 ± 3.72 Hz non-responsive vs. 4.05 ± 3.82 Hz transient, $p = 0.0193$; vs. 5.0 ± 5.4 Hz sustained, $p = 2.91e–5$; transient vs. sustained, $p = 0.0678$; $n = 503$ non-responsive cells, 88 transient, 86 sustained cells in 33 mice, LMEM with Bonferroni correction; Figure 3C). We also examined the degree of correlated firing within groups, finding that transient cells had significantly greater pairwise correlations than either non-responsive or sustained cells (0.29 ± 0.15 transient cells vs. 0.104 ± 0.14 non-responsive cells, $p = 5.59e–39$; vs. 0.08 ± 0.14 sustained cells, $p = 3.16e–17$; non-responsive vs. sustained, $p = 0.0045$; $n = 503$ non-responsive cells, 88 transient, 86 sustained cells in 33 mice, LMEM with Bonferroni correction; Figure 3D).

To quantify the sensitivity of MEC neuronal activity to variation in behavioral state, we calculated a modulation index (MI; STAR Methods) for both locomotion and pupil diameter.[32,33] The majority of neurons exhibited increased firing relative to baseline during locomotion, with transient cells having a significantly greater modulation than either non-responsive or sustained cells (transient MI = 0.19 ± 0.18 vs. non-responsive MI = 0.078 ± 0.28, $p = 0.0069$; vs. sustained MI = 0.05 ± 0.21, $p = 0.0061$; non-responsive vs. sustained $p = 0.27$; $n = 35$ transient, 168 non-responsive, 49 sustained cells in 14 mice, LMEM with Bonferroni correction; Figure 3E). These differences were also apparent when comparing firing rates at locomotion onset across the three groups (Figure 3E). Activity of most cells showed modestly increased activity during changes in arousal, as measured by varying pupil diameter, which did not differ significantly across the different groups (Figure S3).

We next compared visually evoked activity across the different subpopulations, finding that transient cells exhibited a modestly but significantly greater SNR (Figure S3). However, in contrast to spontaneous activity, neither population showed significant modulation of visual responses with variation in either locomotion or pupil diameter (Figure S3). We also calculated pairwise noise correlations for simultaneously recorded cells (STAR Methods), a metric thought to reflect the degree of shared synaptic connectivity or common input.[34] Like spontaneous correlation results, we found that noise correlations were significantly higher between transient versus sustained cells (0.24 ± 0.23 transient vs. 0.08 ± 0.28 sustained, $p = 5.38e–9$, 88 transient, 88 sustained cells in 33 mice, LMEM; Figure 3F), suggesting that this group may comprise a distinct and more strongly interconnected subpopulation.

Within the MEC, theta oscillations (6–12 Hz) in the LFP organize the timing of spike output from individual neurons and may link behavior to activity patterns of neuronal ensembles.[16]

Moreover, previous studies support the hypothesis that the grid cells pattern requires theta oscillation for shaping precise periodic spatial firing in the entorhinal cortex.[35,36] Interestingly, visual stimulation modestly increased LFP power in this range (Figure S3). We further examined the phase locking of single neurons to the ongoing theta oscillation. For spontaneous activity, non-responsive cells exhibited significantly stronger phase locking in comparison to transient or sustained cells (kappa = 0.38 ± 0.34 non-responsive vs. 0.25 ± 0.18 transient, $p = 0.003$; vs. 0.25 ± 0.20 sustained, $p = 0.055$; transient vs. sustained $p = 0.3592$; LMEM with Bonferroni correction, $n = 173$ non-responsive cells, 137 transient, 52 sustained cells in 15 mice). However, visual input significantly enhanced theta phase locking for both transient (kappa = 0.45 ± 0.24, $p = 2.674e–7$, paired LMEM $n = 37$ transient cells in 15 mice) and sustained (kappa = 0.42 ± 0.35, $p = 2.95e–5$, paired LMEM $n = 352$ sustained cells; Figure 3G). Visual stimulation did not alter the preferred theta phase angle for either population (Figure S3).

The RSC drives visual responses in the MEC

We next investigated which afferent inputs to the MEC might contribute to visual responses. Fluorescent retrograde tracing from the dorsal MEC demonstrated the presence of monosynaptic inputs arising from both primary and higher-order visual areas in hemispheres ipsilateral and contralateral to the injection site (Figures 4A and 4B). We observed the strongest retrograde labeling in the RSC (Figure 4B; RSC 24.39 ± 13.68 cells/100 μm^2, primary visual area [VISp] 4.44 ± 4.72 cells/100 μm^2, posteromedial visual area [VISpm] 8.85 ± 5.74 cells/100 μm^2, anteromedial visual area [VISam] 1.31 ± 1.62 cells/100 μm^2, anterolateral visual area [VISal] 0.97 ± 1.80 cells/100 μm^2, lateral visual area [VISl] 0.69 ± 0.9 cells). Confirming these results, anterograde tracing using AAV-driven expression of synaptophysin-tdTomato in the RSC-to-MEC axons led to a high density of labeled boutons concentrated in layers 3 and 5 of the dorsal MEC (Figure S4).

The RSC is a multimodal region that also receives robust input from earlier visual areas.[25,29,37] To determine whether the anatomically strong RSC-to-MEC pathway contributes to visual responses in the latter, we used an AAV vector to express the inhibitory opsin eOPN3[38] in the RSC. We then recorded MEC activity before and during brief green light delivery through an implanted optical fiber. Optogenetic suppression of RSC

terminals robustly reduced MEC visual response magnitude (SNR = 0.68 ± 0.65 baseline vs. 0.12 ± 0.33 during illumination, p = 5.7e–7, LMEM with Bonferroni correction). Initial response magnitudes recovered within 40 min of the last illumination (SNR = 0.54 ± 0.51 post-recovery, p = 6.16e–5 and p = 0.0997 vs. during illumination and baseline, respectively, LMEM with Bonferroni correction; Figures 4D and 4E). Optogenetic suppression of RSC afferents did not affect the spontaneous firing rate of MEC neurons (1.52 ± 1.39 Hz baseline; 2.03 ± 2.18 Hz during illumination; 1.62 ± 1.96 Hz post recovery, p = 0.087 and p = 0.1373, respectively, n = 22 cells in 4 mice; Figure 4E). Furthermore, optical stimulation through the implanted fiber in the absence of eOPN3 expression did not alter MEC activity (Figure S4). Finally, RSC terminal suppression did not change the adaptation ratio of individual MEC neurons, and the magnitude of response suppression did not vary between transient and sustained populations (Figure S4). Overall, these results demonstrate that RSC inputs are a primary pathway carrying visual information to the MEC.

DISCUSSION

In the present study, we found that single neurons in the MEC robustly respond to simple visual stimuli that are not coupled to specific task or navigation demands. Indeed, like other higher-order visual areas, responsive MEC cells exhibited contrast sensitivity and large receptive fields but minimal tuning for other stimulus features, such as orientation, spatial frequency, and motion.[39] These results suggest that associations between external visual cues and internal representations of the environment necessary for cognitive mapping may arise either within or downstream of the MEC.

Visually responsive cells were present throughout the dorsal MEC but were primarily observed within layer 3 (more than twice as many labeled cells were observed in layer 3 versus layer 5), a conclusion supported by activity-dependent labeling using both FosTRAP mice and photoconversion of CaMPARI2.[30,31] Moreover, approximately 30% of CaMPARI2-labeled cells were positive for the molecular marker Ctip2. The functional biology of MEC layer 3 is less well understood than that of layer 2 or 5, comprising a population of excitatory cells projecting to both the CA1 and the subiculum with collaterals to the contralateral MEC.[25,40] Indeed, layer 3 outputs target apical dendrites of CA1 pyramidal neurons, suggesting that they may provide a mechanism for environmental cues to influence or support place cells.[41–44] Consistent with this idea, silencing MEC output produces an expansion of CA1 place fields.[41–43] Nevertheless, prior work found that layer 3 neurons were only modestly coupled to theta rhythmicity and discharged in spatially irregular patterns, with little organization into grid or border patterns that are seen more robustly in layer 2.[40] In combination, our results and these previous findings suggest that MEC layer 3 may be primarily engaged in channeling afferent sensory information to other entorhinal and hippocampal circuits in conjunction with other spatial representations of the environment.[45,46]

MEC neurons varied in their visual response dynamics, with individual cells falling along a continuum of transient versus sustained activity during the presentation of the stimulus. Work in primates suggests that motion-sensitive dorsal visual stream pathways are dominated by transient dynamics, while ventral stream pathways exhibit both transient

and sustained channels.[39,47] Thus, these varied response profiles in the MEC may reflect distinct roles in encoding aspects of the visual scene. In our dataset, transient cells most sensitive to stimulus onset exhibited significantly larger visual response magnitudes, were more modulated by locomotion, and were more correlated within group in comparison to sustained cells, suggesting that these two broad functional categories may correspond to different subpopulations of neurons within the MEC, with distinct long-range and/or local connectivity. *Ex vivo* recordings indicate that recurrent connectivity is considerably stronger in layer 3 versus superficial layer 2 of the MEC,[48] suggesting the potential for selective amplification of afferent visual inputs by specific subpopulations. It is intriguing to speculate that transient and sustained cells may be divided into Ctip2-positive and -negative populations, respectively, with differing degrees of recurrent synaptic connections.

Our optogenetic results indicate that projections to the MEC from the RSC make a major contribution to entorhinal visually evoked activity, consistent with previous anatomical and *ex vivo* electrophysiological studies.[25,29,37] The RSC receives direct sensory inputs from lower-level visual areas,[49–51] and RSC neurons can encode visual landmark information during navigation in a virtual environment.[22] In addition, cells in the RSC may represent relationships between behaviorally salient environmental cues,[22–24] though whether this property arises in the RSC or is inherited from other areas is unclear. As our results show that MEC neurons can encode simple visual stimuli, and the MEC also sends a return projection back to the RSC, it is possible that associations between stimuli and with behaviorally salient cues are formed within the hippocampal formation and then directed back to the neocortex. Interestingly, MEC neurons showed a modest bias for contralateral visual stimuli, similar to contralateral sensitivity for egocentric boundary cells in the RSC.[23] Notably, optogenetic suppression of RSC inputs did not alter the adaptation of visual responses in the MEC (transient versus sustained), again suggesting that these dynamics reflect local circuit connectivity rather than distinct afferent inputs. We hypothesize that differential connectivity of diverse GABAergic interneurons within the MEC may be a key mechanism in determining the degree of visual response adaptation across cellular subpopulations.[52–54]

Visual information is critical for accurate navigation of the environment,[5,11–13] and visual inputs influence both place and grid cells during exploration.[4,11,12,15,16] Similarly, loss of visual information can alter environment-specific activity in both the hippocampus and MEC.[12,14,15] Computational studies suggest that visual signals may serve as a source of error correction during path integration.[11,17–19] In addition to directly encoding visual stimuli, we also find that visual inputs increase the phase locking of MEC neurons to ongoing theta oscillations. Indeed, theta-band activity is associated with active navigation, coordinating grid cell activity, and influencing synaptic plasticity at entorhinal-hippocampal connections.[16,35,36,55,56] Thus, visual signals may indirectly regulate a variety of circuit dynamics central to navigation and memory formation.

MEC neurons exhibit a variety of navigation-specific dynamics, variously encoding spatial grids that tile the local environment, regional edges or borders, specific landmarks, task timing, and locomotion speed. These neuronal dynamics are largely influenced by environmental novelty, which reorganizes neuronal spatial pattern.[57,58] Direct visual

integration could help to synchronize the hippocampal spatial representation with the surrounding environment.[59] The present work was carried out in animals not actively navigating; it will be extremely interesting to explore whether MEC neurons responsive to visual cues also exhibit coding for these other environmental features or comprise a wholly distinct population. Similarly, the impact of discrete visual stimulus features on other navigation encoding properties of MEC neurons is largely unknown. Future studies taking advantage of high-density recordings in mice exploring virtual environments will be critical for addressing the intersection of such representations within the MEC.

Limitations of the study

Although our results support an important role for the RSC inputs in relaying visual information to the MEC, we cannot exclude additional functional contributions from other cortical areas, including primary and higher-order visual areas and the postrhinal cortex.[3,55] Additionally, our study was carried out in awake, head-fixed animals not actively navigating. The relationship of visual responses to entorhinal encoding of other environmental features awaits further study. Finally, the local circuit mechanisms regulating visual response dynamics, including the contribution of diverse GABAergic interneurons, presently remain unknown.

STAR★METHODS

RESOURCE AVAILABILITY

Lead contact—Further information and requests for resources and reagents should be directed to and will be fulfilled by the lead contact, Pr. Michael Higley (michael.higley@yale.edu).

Materials availability—This study did not generate new reagents.

Data and code availability

- All data reported in this paper will be shared by the lead contact upon request.

- Original code used in the present study can be found at https://github.com/cardin-higley-lab/Dubanet_Higley_2024.

- Any additional information required to reanalyze the data reported in this work paper is available from the lead contact upon request.

EXPERIMENTAL MODEL AND STUDY PARTICIPANT DETAILS

Adult (P60–100) male C57Bl/6 (Charles River), Ai34D synaptophysin-tdTomato reporter (B6; 129S-Gt(ROSA)26Sortm34.1(CAG-Syp/tdTomato)Hze/J, JAX stock no. 012570), and double heterozygous FosTRAP (Fos-tm2.1-icre-ERT2, JAX stock no. 030323 crossed to B6.Cg-Gt-ROSA-26SOR-tm9-CAG-tdTomato, JAX stock no. 007909 reporter) mice were kept on a 12-h light/dark cycle and provided with food and water *ad libitum*. Experiments were carried out in the light phase of the cycle. All animal handling and experiments were performed according to the ethical guidelines of the Institutional Animal Care and Use Committee of the Yale University School of Medicine.

METHOD DETAILS

Surgical procedures—For all surgical procedures, mice were anesthetized with 1–2% isoflurane and maintained at 37°C for the duration of the surgery. For head-post implantation, the scalp was resected and the skull cleaned with saline. A surgical screw was implanted in the skull anterior to bregma, and a custom titanium headpost was secured above the bregmoid suture with Vetbond. Ground and reference wires were inserted above the cerebellum. A circular plastic ring (~1.5mm diameter) secured on the skull above the left MEC (AP: 0.5mm anterior to the lambdoid suture, LM: 4.2mm) with Vetbond. Implant components were then covered with dental cement (Metabond, Parkell Industries). FosTRAP experiments were similar, but reference electrodes and the circular plastic ring were omitted.

For retrograde tracing, a small craniotomy was made over the left MEC followed by injection of 200 nL Alexa Fluor 555-conjugated cholera toxin subunit B (ThermoFisher). For optogenetic manipulation of RSC terminals within the MEC, a craniotomy was first made over the left RSC (AP: –4 mm, LM: –0.6mm) followed by injection of 200nL AAV9-CaMKII-Cre (1.0e12 gc/mL, Addgene). Two weeks following this initial injection, a similar procedure was used to inject 200nL AAV5-hSyn1-SIO-eOPN3-mScarlet-WPRE (3.4ê12 gc/mL, Addgene) into the RSC. In the same procedure, a headpost and reference electrodes were implanted as above. For CaMPARI 2.0 tagging of visually responsive cells, 200nL AAV1-hSyn-NES-his-CaMPARI2-WPRE-SV40 (2.5e12 gc/mL, Addgene) was injected into the left MEC. Following injection, a tapered tip optical fiber (DoricLenses) was inserted into the MEC and affixed with the head-post to the skull with dental cement. For anterograde tracing, Ai34D reporter mice were injected with 200nL of AAV.hSyn.Cre.WPRE.hGH (1.9e12 gc/mL, Addgene) into the left RSC at the same coordinates. At the conclusion of all experiments, animals were deeply anesthetized with isoflurane and perfused transcardially with 4% paraformaldehyde in Sorenson's buffer.

Electrophysiological recordings—Mice were habituated to handling and head fixation on a freely-moving running wheel for 3–5 days prior to electrophysiological recordings. On the day of recording, a small craniotomy was performed above the left MEC under isoflurane anesthesia, centered on the implanted plastic ring. After surgery, mice were allowed to recover for >2h in their home cage followed by head-fixation on the wheel. The ring surrounding the craniotomy was filled with artificial cerebrospinal fluid (in mM: 135 NaCl, 5 KCl, 5 HEPES, 1 MgCl2, 1.8 CaCl2, adjusted to pH 7.3). For recordings, an A1×32-Poly3-10mm-25, 32 channel probe (Neuronexus) or an NN1620 optotrode (Neuronexus) were connected to a recording apparatus (DigitalLynx system, Neuralynx), dipped into DiI Invitrogen), and lowered into the MEC. Data were filtered from 0.1 to 9000Hz and acquired at 40 kHz sampling rate. Wheel sensor data and time stamps for facial video and visual stimulation were acquired simultaneously.

Behavioral monitoring—For all experiments, a magnetic angle sensor (Digikey) attached to the wheel continuously monitored wheel motion. In addition, the face was illuminated with an infrared LED bank and imaged with a miniature CMOS camera (Blackfly s-USB3, Flir) with a frame rate of 10 Hz.

Visual stimulation—Visual stimuli were generated with custom scripts using the Psychtoolbox MATLAB extension (Kleiner et al., 2007) and displayed on a 17″ by 9.5″ monitor situated 20 cm in front of the animal (binocular experiment) or 15 cm from the right eye (all other recording sessions). Display output was gamma corrected with maximum luminance adjusted to ~140 cd.sr/m2. An iso-luminant, medium-gray background was displayed between visual stimuli. Drifting or static inverting sinusoidal gratings were presented for 1 s and separated by a 4 s intervals. Stimulus properties were varied across distinct experimental cohorts as follows: contrast (2, 40, 100%), spatial frequency (0.01, 0.0275, 0.045, 0.0625, 0.08 cycles/degree), size (5, 10, 40, 100°), orientation (0, 54, 108, 154, 205, 257, 308, 360°). All stimuli were presented at a drift/inverting frequency of 2 cycles/sec. For Retinotopy mapping, visual stimulations were randomly presented at several positions in the visual field (1 s duration, 4 s inter-stimulus interval, 100-degree drifting grating patch, 100% contrast, 0.04 cycles/degree, 0° orientation, 2 Hz cycles/second, 50 presentations per positions).

Activity-dependent labeling of MEC neurons—FosTRAP mice were habituated to handling and head fixation on a fixed wheel for 3–5 days followed by light deprivation for 5 days. Tamoxifen was dissolved at 20 mg/mL in pure ethanol, then mixed 1:4 with sunflower oil at 37°C for 3 h. The tamoxifen solution was injected intraperitoneally at 20 mg/kg right and mice were positioned on a fixed wheel to prevent running. Visual stimuli (300 presentations) were generated as above (1 s on, 4 s inter-stimulus interval, 100-degree drifting grating patch, 100% contrast, 0.04 cycles/degree, 0° orientation, 2 Hz cycles/second). For CaMPARI2.0 labeling, following habituation to handling and head fixation as above, mice were head-fixed on the wheel and a 405 nm LED (Thorlab) was coupled to the implanted optical fiber. Visual stimuli (same as FosTRAP experiments) were presented simultaneously with delivery of 405 nm light (2 mW at the fiber tip). At the conclusion of both FosTRAP and CaMPARI2.0 experiments, animals were deeply anesthetized and perfused transcardially with 4% paraformaldehyde in Sorenson's buffer for histological analysis of labeled cells.

Optogenetic suppression of RSC output—For optogenetic silencing of RSC terminals inside the MEC, a green (554 nm) LED (Thorlabs) was coupled to the implanted fiber and 4 s pulses (5 mW at the fiber tip) were delivered every 60 s during the recording session.

Histological processing—Brains were post-fixed overnight in 4% paraformaldehyde for 24 h followed by storage in Sorenson's buffer. Coronal or sagittal sections (50μm-thick) were prepared with a vibratome (Leica). For CaMPARI2.0 labeling experiments, sections were pre-treated in blocking solution (0.02% BSA, 10% normal goat serum, 0.5% Triton X-100 in Sorenson's buffer) for 4–6 h. Sections were then incubated over night with primary antibodies including mouse anti-CaMPARI-red (1:500, Absolute Antibody) and either guinea pig anti-Ctip2 (1:500, Synaptic Systems), rabbit anti-reelin (1:500, Invitrogen), or rabbit anti-calbindin (1:500, Synaptic Systems) diluted in blocking solution. The following day, sections were washed with Sorenson's buffer and incubated in appropriate secondary antibodies (goat anti-mouse Alexa Fluor 555, goat anti-guinea pig-Alex Fluor 647, goat anti-

rabbit Alexa Fluor 647, Invitrogen) at 1:1000 for 2 h. Sections were rinsed in Sorenson's buffer and mounted on glass slides with Vectashield antifade mounting medium including DAPI (Vector Laboratories). For AAV-Cre/Ai9 anterograde tracing, eOPN3 RSC projection tracing and DiI post-hoc verification of electrodes positions, 50μm sagittal brain sections were mounted with Vectashield antifade mounting medium including DAPI.

QUANTIFICATION AND STATISTICAL ANALYSIS

Histology—For all histological analyses, fields of view were captured via confocal microscope through a 10× objective (Zeiss LSM900). Cells and axonal puncta were identified using the Analyze Particles function in ImageJ version 1.53t and processed with the SHARCQ MATLAB GUI[62] for atlas alignment and calculation of object density per area. CaMPARI2.0 colocalization and fluorescence intensity were identified and quantified with using CellProfiler.[64] Briefly, we identified cell bodies in the 488 nm and 555 nm channels to identify infected and photoconverted cells. We then quantified the colocalization of red cells with secondary antibody labeling in the 647 nm channel.

Behavioral state—Behavioral epochs were identified as in our previous work.[32] Pupil diameter was computed from facial video using FaceMap.[65] First, data were Z-scored within a session and the high and low thresholds corresponding to 60% and 40% quantiles in the data distribution, were extracted for that session. Data were then smoothed using a 1-s window moving-average filter, and epochs during which smoothed data continuously exceeded the high and low Z-thresholds for at least 5 s were considered high and low pupil size, respectively. Wheel position was determined from the output of the linear angle detector. The circular wheel position variable was first transformed to the $[-\pi, \pi]$ interval. The phases were then circularly unwrapped to obtain running distance as a linear variable, and locomotion speed was computed as a differential of distance (m s −1). A change-point detection algorithm detected locomotion onset and offset times based on changes in standard deviation of speed for at least 5s to be considered as locomotion periods.

Electrophysiology—Data were visualized and processed using NeuroScope from the Neurosuite and NDManager software[67] (http://neurosuite.sourceforge.net) and analyzed using MATLAB (MathWorks) built-in or custom-built procedures (FMAToolbox https://github.com/michael-zugaro/FMAToolbox). Single units were extracted and clustered from LFP recordings using kilosort2,[66] with clusters manually verified and refined using the phy-gui (https://github.com/cortex-lab/phy). Pupil diameter and locomotion were interpolated and aligned to the spike time data. Electrophysiology data were analyzed in MATLAB 2021a (Mathworks) using custom scripts. All time-series were down-sampled to 20KHz and aligned. Single unit half-width was computed as the time between half-maximal fall and rise of the negative-going spike peak, and peak-to-trough duration was computed as the time between maximum negative spike peak and the first positive maximum for the average unit waveform over 10,000 spikes.

The spontaneous pairwise correlation coefficient was defined as the covariance of spike counts normalized by the product of the variances of each cell:

$$\rho = \frac{Cov(n1(t), n2(t))}{\sqrt{Var(n1(t))Var(n2(t))}}$$

where n1(t) and n2(t) are spike counts of neuron 1 and 2 for the same time bin t ms (t = 200ms).

For visually evoked activity, individual neuron peri-stimulus time histograms were computed for each stimulus feature combination. Control shuffled histograms were computed by shuffling the interspike intervals 1000 times for each neuron. Neurons were considered positively responding if the mean of the raw PSTH was significantly greater than the mean of the shuffled PSTH during the visual presentation ($p < 0.01$, Student's t-test). Cells were categorized as inhibited when the mean of the raw PSTH was significantly lower than the mean shuffled PSTH (p value < 0.01, Student's t-test). Response magnitudes were quantified as the signal-to-noise ratio (SNR), defined as the difference between the mean firing rate during the stimulus window and the mean firing rate in a 1-s baseline period immediately preceding the stimulus, normalized to the baseline rate. To examine tuning for visual stimulus features, SNR values were plotted against stimulus contrast, size, spatial frequency, and orientation. An orientation selectivity index (OSI) was also calculated as the ratio of (Rpref-Ropp)/(Rpref+Ropp) where Rpref was the response of the preferred orientation (i.e., max response) and Ropp was the response of the opposite orientation. Noise correlations were calculated for each pair of visually responsive cells as the Pearson's correlation coefficient for Z-scored visually-evoked responses in each cell across repeated stimulus presentations.

To quantify the temporal response profile for each cell, we computed an adaptation ratio (AR) for each positively responding neuron as the ratio of the firing rate 400–1000ms after stimulus onset to the firing rate 200–400ms after stimulus onset. Transient and sustained cells were defined as those in the lower and upper quartiles, respectively, of AR across all positively responsive cells.

Change in neural activity associated with variation in behavioral metrics was calculated using a modulation index defined as (FRHigh-FRLow)/(FRHigh+FRLow) where FRHigh is the mean spontaneous or visually-evoked firing rate during either locomotion or large pupil epochs and FRLow is the mean spontaneous or visually evoked firing rate during quiescence or small pupil epochs. As pupil diameter is correlated with locomotion, large pupil epochs that occurred during locomotion were excluded from analysis.

To identify epochs of theta oscillations, the raw recordings were down-sampled to 1250 Hz and the integrated power was calculated for the 4–11Hz (theta) and 1–3Hz (delta) frequency bands using the multi-taper method (1 s time window and 4 tapers) implemented in the Chronux MATLAB toolbox[63] (https://www.mathworks.com/matlabcentral/fileexchange/68537-chronux-analysis-software). Theta periods were defined for epochs in which the theta/delta power ratio was greater than 3 and validated manually using the Sonic Visualizer free software (https://www.sonicvisualiser.org). Within theta epochs, we calculated oscillation phase by divided the signal into 500ms overlapping segments (75%

overlap). Each segment was multiplied by a Hamming window and their Fourier transform was computed (MATLAB function fft). Theta phase was computed in theta periods using the Hilbert transform on band-pass filtered (4–11 Hz) down-sampled LFP. Phase modulation of neurons relative to theta oscillations was tested by using the Rayleigh test (nonuniformity of the circular distribution). When phase modulation was significant ($p < 0.05$), von Mises parameters μ and κ were estimated via maximum likelihood as indices of preferred phase and modulation strength, respectively (CricStat MATLAB tool box, https://www.mathworks.com/matlabcentral/fileexchange/10676-circular-statistics-toolbox-directional-statistics).

Statistics—All statistical analyses were conducted using custom-written scripts in MATLAB. For electrophysiological data, recordings were combined across one or two sessions per animal. Given the nested structure of most datasets (multiple cells per animal), for these analyses we used a linear mixed effects model (LMEM) based on the fitlme function in MATLAB. Experimental variables were treated as fixed effects and individual animal was treated as a random effect. For paired data comparisons, we also used the fitlme function with repeated measures treated as a random effect. A Bonferroni correction was applied for all multiple comparisons analyses. All statistical tests are summarized in Table S1. Results were considered significant for $p < 0.05$. Unless indicated otherwise, all results are presented as mean ± SD. Violin plots were created as described previously (https://www.mathworks.com/matlabcentral/fileexchange/45134-violin-plot, MATLAB Central File Exchange).

Supplementary Material

Refer to Web version on PubMed Central for supplementary material.

ACKNOWLEDGMENTS

REFERENCES

1. Sosa M, and Giocomo LM (2021). Navigating for reward. Nat. Rev. Neurosci 22, 472–487. 10.1038/s41583-021-00479-z. [PubMed: 34230644]

2. Buzsaki G, and Moser EI (2013). Memory, navigation and theta rhythm in the hippocampal-entorhinal system. Nat. Neurosci 16, 130–138. 10.1038/nn.3304. [PubMed: 23354386]

3. Campbell MG, and Giocomo LM (2018). Self-motion processing in visual and entorhinal cortices: inputs, integration, and implications for position coding. J. Neurophysiol 120, 2091–2106. 10.1152/jn.00686.2017. [PubMed: 30089025]

4. Hafting T, Fyhn M, Molden S, Moser MB, and Moser EI (2005). Microstructure of a spatial map in the entorhinal cortex. Nature 436, 801–806. 10.1038/nature03721. [PubMed: 15965463]

5. O'Keefe J, and Dostrovsky J (1971). The hippocampus as a spatial map. Preliminary evidence from unit activity in the freely-moving rat. Brain Res. 34, 171–175. [PubMed: 5124915]

6. Diehl GW, Hon OJ, Leutgeb S, and Leutgeb JK (2017). Grid and Nongrid Cells in Medial Entorhinal Cortex Represent Spatial Location and Environmental Features with Complementary Coding Schemes. Neuron 94, 83–92.e6. 10.1016/j.neuron.2017.03.004. [PubMed: 28343867]

7. Heys JG, and Dombeck DA (2018). Evidence for a subcircuit in medial entorhinal cortex representing elapsed time during immobility. Nat. Neurosci 21, 1574–1582. 10.1038/s41593-018-0252-8. [PubMed: 30349104]

8. Kropff E, Carmichael JE, Moser MB, and Moser EI (2015). Speed cells in the medial entorhinal cortex. Nature 523, 419–424. 10.1038/nature14622. [PubMed: 26176924]

9. Hinman JR, Brandon MP, Climer JR, Chapman GW, and Hasselmo ME (2016). Multiple Running Speed Signals in Medial Entorhinal Cortex. Neuron 91, 666–679. 10.1016/j.neuron.2016.06.027. [PubMed: 27427460]

10. Dannenberg H, Lazaro H, Nambiar P, Hoyland A, and Hasselmo ME (2020). Effects of visual inputs on neural dynamics for coding of location and running speed in medial entorhinal cortex. Elife 9, e62500. 10.7554/eLife.62500. [PubMed: 33300873]

11. Kinkhabwala AA, Gu Y, Aronov D, and Tank DW (2020). Visual cuerelated activity of cells in the medial entorhinal cortex during navigation in virtual reality. Elife 9, e43140. 10.7554/eLife.43140. [PubMed: 32149601]

12. Campbell MG, Ocko SA, Mallory CS, Low IIC, Ganguli S, and Giocomo LM (2018). Principles governing the integration of landmark and self-motion cues in entorhinal cortical codes for navigation. Nat. Neurosci 21, 1096–1106. 10.1038/s41593-018-0189-y. [PubMed: 30038279]

13. Robinson L, Bridge H, and Riedel G (2001). Visual discrimination learning in the water maze: a novel test for visual acuity. Behav. Brain Res 119, 77–84. 10.1016/s0166-4328(00)00334-x. [PubMed: 11164528]

14. Chen G, Manson D, Cacucci F, and Wills TJ (2016). Absence of Visual Input Results in the Disruption of Grid Cell Firing in the Mouse. Curr. Biol 26, 2335–2342. 10.1016/j.cub.2016.06.043. [PubMed: 27498565]

15. Perez-Escobar JA, Kornienko O, Latuske P, Kohler L, and Allen K (2016). Visual landmarks sharpen grid cell metric and confer context specificity to neurons of the medial entorhinal cortex. Elife 5, e16937. 10.7554/eLife.16937. [PubMed: 27449281]

16. Buzsaki G (2005). Theta rhythm of navigation: link between path integration and landmark navigation, episodic and semantic memory. Hippocampus 15, 827–840. 10.1002/hipo.20113. [PubMed: 16149082]

17. Burgess N, Barry C, and O'Keefe J (2007). An oscillatory interference model of grid cell firing. Hippocampus 17, 801–812. 10.1002/hipo.20327. [PubMed: 17598147]

18. Fuhs MC, and Touretzky DS (2006). A spin glass model of path integration in rat medial entorhinal cortex. J. Neurosci 26, 4266–4276. 10.1523/jneurosci.4353-05.2006. [PubMed: 16624947]

19. Bush D, Barry C, and Burgess N (2014). What do grid cells contribute to place cell firing? Trends Neurosci. 37, 136–145. 10.1016/j.tins.2013.12.003. [PubMed: 24485517]

20. Pinke D, Issa JB, Dara GA, Dobos G, and Dombeck DA (2023). Full field-of-view virtual reality goggles for mice. Neuron 111, 3941–3952.e6. 10.1016/j.neuron.2023.11.019. [PubMed: 38070501]

21. Aronov D, and Tank DW (2014). Engagement of neural circuits underlying 2D spatial navigation in a rodent virtual reality system. Neuron 84, 442–456. 10.1016/j.neuron.2014.08.042. [PubMed: 25374363]

22. Fischer LF, Mojica Soto-Albors R, Buck F, and Harnett MT (2020). Representation of visual landmarks in retrosplenial cortex. Elife 9, e51458. 10.7554/eLife.51458. [PubMed: 32154781]

23. Alexander AS, Carstensen LC, Hinman JR, Raudies F, Chapman GW, and Hasselmo ME (2020). Egocentric boundary vector tuning of the retrosplenial cortex. Sci. Adv 6, eaaz2322. 10.1126/sciadv.aaz2322. [PubMed: 32128423]

24. van Wijngaarden JB, Babl SS, and Ito HT (2020). Entorhinal-retrosplenial circuits for allocentric-egocentric transformation of boundary coding. Elife 9, e59816. 10.7554/eLife.59816. [PubMed: 33138915]

25. Witter MP, Doan TP, Jacobsen B, Nilssen ES, and Ohara S (2017). Architecture of the Entorhinal Cortex A Review of Entorhinal Anatomy in Rodents with Some Comparative Notes. Front. Syst. Neurosci 11, 46. 10.3389/fnsys.2017.00046. [PubMed: 28701931]

26. Burwell RD, and Amaral DG (1998). Cortical afferents of the perirhinal, postrhinal, and entorhinal cortices of the rat. J. Comp. Neurol 398, 179–205. 10.1002/(sici)1096-9861(19980824)398:2<179::aid-cne3>3.0.co;2-y. [PubMed: 9700566]

27. Jones BF, and Witter MP (2007). Cingulate cortex projections to the parahippocampal region and hippocampal formation in the rat. Hippocampus 17, 957–976. 10.1002/hipo.20330. [PubMed: 17598159]

28. Wang Q, and Burkhalter A (2007). Area map of mouse visual cortex. J. Comp. Neurol 502, 339–357. 10.1002/cne.21286. [PubMed: 17366604]

29. Czajkowski R, Sugar J, Zhang SJ, Couey JJ, Ye J, and Witter MP (2013). Superficially projecting principal neurons in layer V of medial entorhinal cortex in the rat receive excitatory retrosplenial input. J. Neurosci 33, 15779–15792. 10.1523/JNEUROSCI.2646-13.2013. [PubMed: 24089485]

30. Guenthner CJ, Miyamichi K, Yang HH, Heller HC, and Luo L (2013). Permanent genetic access to transiently active neurons via TRAP: targeted recombination in active populations. Neuron 78, 773–784. 10.1016/j.neuron.2013.03.025. [PubMed: 23764283]

31. Moeyaert B, Holt G, Madangopal R, Perez-Alvarez A, Fearey BC, Trojanowski NF, Ledderose J, Zolnik TA, Das A, Patel D, et al. (2018). Improved methods for marking active neuron populations. Nat. Commun 9, 4440. 10.1038/s41467-018-06935-2. [PubMed: 30361563]

32. Lohani S, Moberly AH, Benisty H, Landa B, Jing M, Li Y, Higley MJ, and Cardin JA (2022). Spatiotemporally heterogeneous coordination of cholinergic and neocortical activity. Nat. Neurosci 25, 1706–1713. 10.1038/s41593-022-01202-6. [PubMed: 36443609]

33. Vinck M, Batista-Brito R, Knoblich U, and Cardin JA (2015). Arousal and locomotion make distinct contributions to cortical activity patterns and visual encoding. Neuron 86, 740–754. 10.1016/j.neuron.2015.03.028. [PubMed: 25892300]

34. Cohen MR, and Kohn A (2011). Measuring and interpreting neuronal correlations. Nat. Neurosci 14, 811–819. 10.1038/nn.2842. [PubMed: 21709677]

35. Brandon MP, Bogaard AR, Libby CP, Connerney MA, Gupta K, and Hasselmo ME (2011). Reduction of theta rhythm dissociates grid cell spatial periodicity from directional tuning. Science 332, 595–599. 10.1126/science.1201652. [PubMed: 21527714]

36. Koenig J, Linder AN, Leutgeb JK, and Leutgeb S (2011). The spatial periodicity of grid cells is not sustained during reduced theta oscillations. Science 332, 592–595. 10.1126/science.1201685. [PubMed: 21527713]

37. Simonsen ØW, Czajkowski R, and Witter MP (2022). Retrosplenial and subicular inputs converge on superficially projecting layer V neurons of medial entorhinal cortex. Brain Struct. Funct 227, 2821–2837. 10.1007/s00429-022-02578-8. [PubMed: 36229654]

38. Mahn M, Saraf-Sinik I, Patil P, Pulin M, Bitton E, Karalis N, Bruentgens F, Palgi S, Gat A, Dine J, et al. (2021). Efficient optogenetic silencing of neurotransmitter release with a mosquito rhodopsin. Neuron 109, 1621–1635.e8. 10.1016/j.neuron.2021.03.013. [PubMed: 33979634]

39. Van Essen DC, and Gallant JL (1994). Neural mechanisms of form and motion processing in the primate visual system. Neuron 13, 1–10. 10.1016/0896-6273(94)90455-3. [PubMed: 8043270]

40. Tang Q, Ebbesen CL, Sanguinetti-Scheck JI, Preston-Ferrer P, Gundlfinger A, Winterer J, Beed P, Ray S, Naumann R, Schmitz D, et al. (2015). Anatomical Organization and Spatiotemporal Firing Patterns of Layer 3 Neurons in the Rat Medial Entorhinal Cortex. J. Neurosci 35, 12346–12354. 10.1523/JNEUROSCI.0696-15.2015. [PubMed: 26354904]

41. Brun VH, Leutgeb S, Wu HQ, Schwarcz R, Witter MP, Moser EI, and Moser MB (2008). Impaired spatial representation in CA1 after lesion of direct input from entorhinal cortex. Neuron 57, 290–302. 10.1016/j.neuron.2007.11.034. [PubMed: 18215625]

42. Schlesiger MI, Cannova CC, Boublil BL, Hales JB, Mankin EA, Brandon MP, Leutgeb JK, Leibold C, and Leutgeb S (2015). The medial entorhinal cortex is necessary for temporal organization of hippocampal neuronal activity. Nat. Neurosci 18, 1123–1132. 10.1038/nn.4056. [PubMed: 26120964]

43. Hales JB, Schlesiger MI, Leutgeb JK, Squire LR, Leutgeb S, and Clark RE (2014). Medial entorhinal cortex lesions only partially disrupt hippocampal place cells and hippocampus-dependent place memory. Cell Rep. 9, 893–901. 10.1016/j.celrep.2014.10.009. [PubMed: 25437546]

44. Steward O, and Scoville SA (1976). Cells of origin of entorhinal cortical afferents to the hippocampus and fascia dentata of the rat. J. Comp. Neurol 169, 347–370. 10.1002/cne.901690306. [PubMed: 972204]

45. Sargolini F, Fyhn M, Hafting T, McNaughton BL, Witter MP, Moser MB, and Moser EI (2006). Conjunctive representation of position, direction, and velocity in entorhinal cortex. Science 312, 758–762. 10.1126/science.1125572. [PubMed: 16675704]

46. Bowler JC, and Losonczy A (2023). Direct cortical inputs to hippocampal area CA1 transmit complementary signals for goal-directed navigation. Neuron 111, 4071–4085.e6. 10.1016/j.neuron.2023.09.013. [PubMed: 37816349]

47. Stigliani A, Jeska B, and Grill-Spector K (2019). Differential sustained and transient temporal processing across visual streams. PLoS Comput. Biol 15, e1007011. 10.1371/journal.pcbi.1007011. [PubMed: 31145723]

48. Dhillon A, and Jones RS (2000). Laminar differences in recurrent excitatory transmission in the rat entorhinal cortex in vitro. Neuroscience 99, 413–422. 10.1016/s0306-4522(00)00225-6. [PubMed: 11029534]

49. Vann SD, Aggleton JP, and Maguire EA (2009). What does the retrosplenial cortex do? Nat. Rev. Neurosci 10, 792–802. 10.1038/nrn2733. [PubMed: 19812579]

50. Sit KK, and Goard MJ (2023). Coregistration of heading to visual cues in retrosplenial cortex. Nat. Commun 14, 1992. 10.1038/s41467-023-37704-5. [PubMed: 37031198]

51. Mitchell AS, Czajkowski R, Zhang N, Jeffery K, and Nelson AJD (2018). Retrosplenial cortex and its role in spatial cognition. Brain Neurosci. Adv 2, 2398212818757098. 10.1177/2398212818757098.

52. Couey JJ, Witoelar A, Zhang SJ, Zheng K, Ye J, Dunn B, Czajkowski R, Moser MB, Moser EI, Roudi Y, and Witter MP (2013). Recurrent inhibitory circuitry as a mechanism for grid formation. Nat. Neurosci 16, 318–324. 10.1038/nn.3310. [PubMed: 23334580]

53. Martinez JJ, Rahsepar B, and White JA (2017). Anatomical and Electrophysiological Clustering of Superficial Medial Entorhinal Cortex Interneurons. eNeuro 4, ENEURO.0263–16.2017. 10.1523/ENEURO.0263-16.2017.

54. Varga C, Lee SY, and Soltesz I (2010). Target-selective GABAergic control of entorhinal cortex output. Nat. Neurosci 13, 822–824. 10.1038/nn.2570. [PubMed: 20512133]

55. Yang S, Lee DS, Chung CH, Cheong MY, Lee CJ, and Jung MW (2004). Long-term synaptic plasticity in deep layer-originated associational projections to superficial layers of rat entorhinal cortex. Neuroscience 127, 805–812. 10.1016/j.neuroscience.2004.06.001. [PubMed: 15312893]

56. Mizuseki K, and Buzsaki G (2014). Theta oscillations decrease spike synchrony in the hippocampus and entorhinal cortex. Philos. Trans. R. Soc. Lond. B Biol. Sci 369, 20120530. 10.1098/rstb.2012.0530.

57. Barry C, Ginzberg LL, O'Keefe J, and Burgess N (2012). Grid cell firing patterns signal environmental novelty by expansion. Proc. Natl. Acad. Sci. USA 109, 17687–17692. 10.1073/pnas.1209918109. [PubMed: 23045662]

58. Munn RGK, Mallory CS, Hardcastle K, Chetkovich DM, and Giocomo LM (2020). Entorhinal velocity signals reflect environmental geometry. Nat. Neurosci 23, 239–251. 10.1038/s41593-019-0562-5. [PubMed: 31932764]

59. Raudies F, Mingolla E, and Hasselmo ME (2012). Modeling the influence of optic flow on grid cell firing in the absence of other cues1. J. Comput. Neurosci 33, 475–493. 10.1007/s10827-012-0396-6. [PubMed: 22555390]

60. Molter C, O'Neill J, Yamaguchi Y, Hirase H, and Leinekugel X (2012). Rhythmic modulation of theta oscillations supports encoding of spatial and behavioral information in the rat hippocampus. Neuron 75, 889–903. 10.1016/j.neuron.2012.06.036. [PubMed: 22958828]

61. Kleiner M, Brainard D, Pelli D, Ingling A, Murray R, and Broussard C (2007). What's new in psychtoolbox-3. Perception 36, 1–16.

62. Kristoffer L, Annie L, Emily DP, Connor M, Dillon JM, Jian Wei T, Joseph D, and David HR (2022). A Semi-Automated Workflow for Brain Slice Histology Alignment, Registration, and Cell Quantification (SHARCQ). eneuro 9, ENEURO.0483–0421.2022. 10.1523/ENEURO.0483-21.2022.

63. Bokil H, Andrews P, Kulkarni JE, Mehta S, and Mitra PP (2010). Chronux: a platform for analyzing neural signals. J. Neurosci. Methods 192, 146–151. 10.1016/j.jneumeth.2010.06.020. [PubMed: 20637804]

64. Stirling DR, Swain-Bowden MJ, Lucas AM, Carpenter AE, Cimini BA, and Goodman A (2021). CellProfiler 4: improvements in speed, utility and usability. BMC Bioinf. 22, 433. 10.1186/s12859-021-04344-9.

65. Syeda A, Zhong L, Tung R, Long W, Pachitariu M, and Stringer C (2022). Facemap: a framework for modeling neural activity based on orofacial tracking. bioRxiv. 10.1101/2022.11.03.515121.

66. Pachitariu M, Steinmetz N, Kadir S, Carandini M, and Kenneth DH (2016). Kilosort: realtime spike-sorting for extracellular electrophysiology with hundreds of channels. bioRxiv. 10.1101/061481.

67. Hazan L, Zugaro M, and Buzsáki G (2006). Klusters, NeuroScope, NDManager: a free software suite for neurophysiological data processing and visualization. J. Neurosci. Methods 155, 207–216. [PubMed: 16580733]

Author Manuscript

Author Manuscript

Author Manuscript

Author Manuscript

Highlights

- Single neurons in the MEC respond robustly to simple visual stimuli

- Visually driven MEC cells can be grouped by response dynamics and molecular markers

- Suppression of retrosplenial inputs to the MEC strongly inhibits visual responses
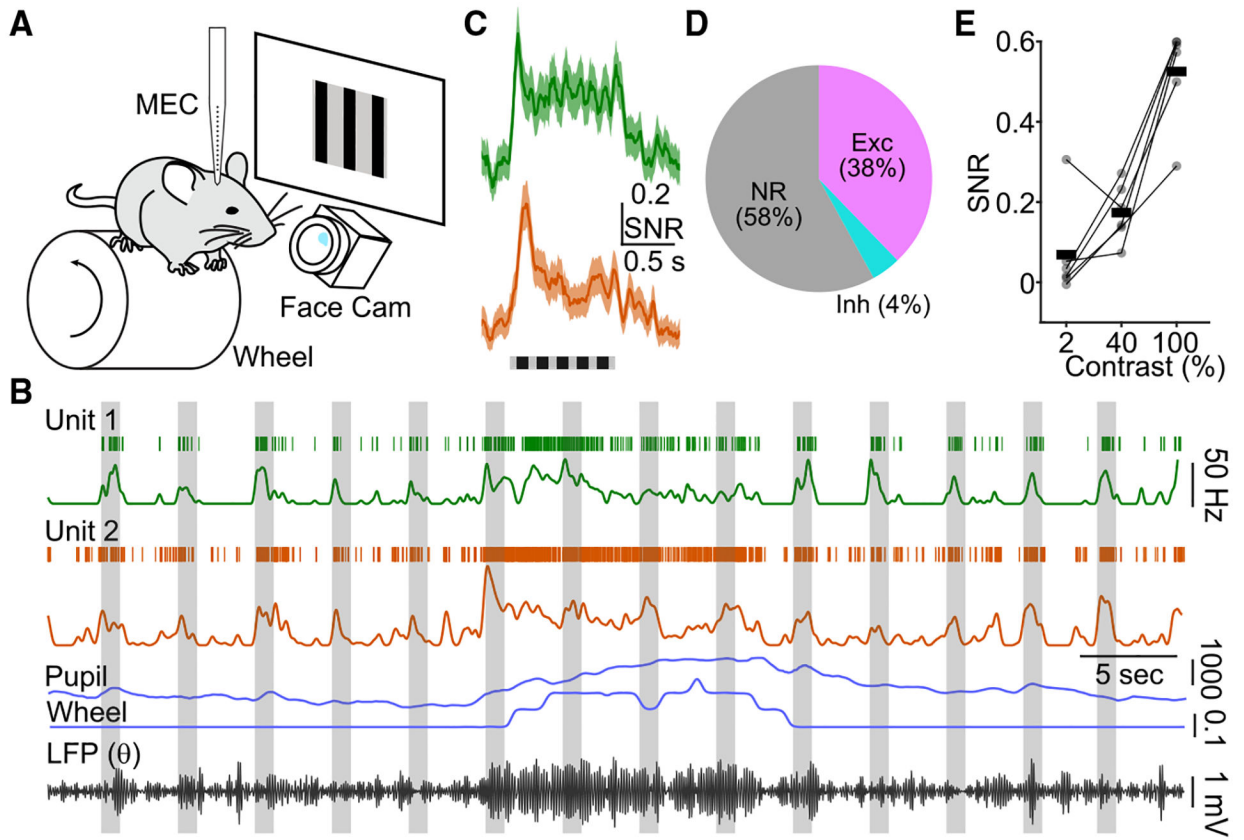
Figure 1. MEC neurons are responsive to simple visual stimuli
(A) Schematic illustrating the setup for head-fixed recording in the awake mouse.

(B) Example recordings for two single units (green and orange) in the dorsal MEC. For each unit, the upper trace shows a raster plot of single spikes, and the lower trace shows the instantaneous firing rate (0.5-s smoothing kernel). Simultaneous pupil diameter and locomotion speed are shown below (a.u. and m/s respectively, blue). Theta band activity (4–12 Hz filtered local field potential) is shown at the bottom. Visual stimuli are indicated by gray vertical bars.

(C) Average ($n = 100$ trials) visually evoked response for units shown in (B). Data show a peristimulus time histogram smoothed with a 50-ms moving window (mean ± SEM, vertical bar 0.2 SNR, horizontal bar 0.5 s).

(D) Proportion of all recorded neurons exhibiting increased or suppressed firing during visual stimulation ($n = 892$ cells in 33 mice).

(E) Population data showing individual and averaged ($n = 6$ mice, 119 cells) visually evoked SNR values as a function of stimulus contrast.

Unless indicated otherwise, all results are presented as mean ± SD.
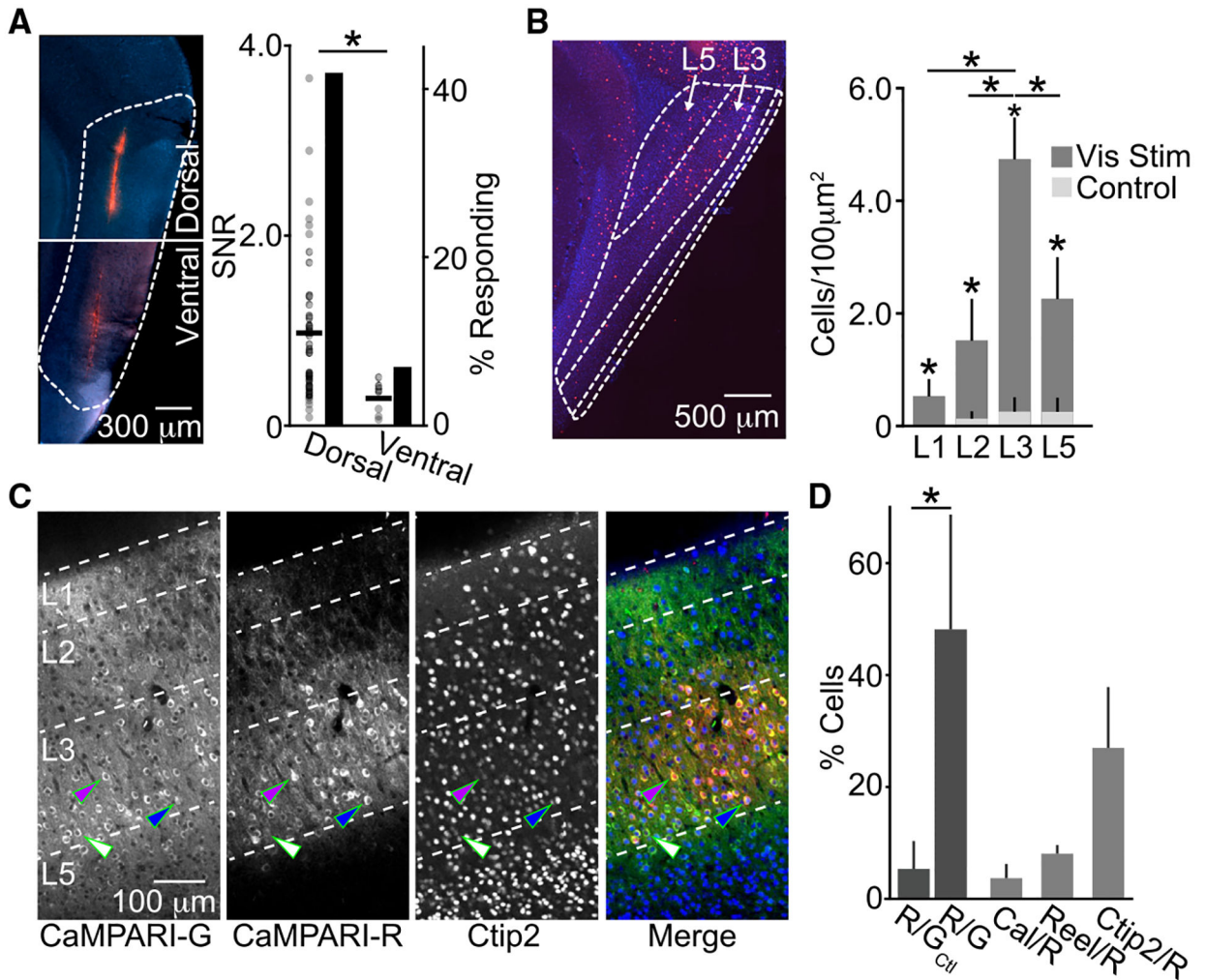
Figure 2. Anatomical and molecular diversity across visually responsive MEC neurons

(A) Left: DiI labeling of the recording electrode track in the dorsal and ventral MEC (scale bar, 300 μm). Right: visual SNR values (dots) and percentage of visually responsive cells (bars) are shown for the dorsal versus ventral MEC recording sites ($n = 3$ mice, 42 cells in the dorsal and 8 cells in the ventral MEC, LMEM $p < 0.05$).

(B) Left: example image showing FosTRAP-labeled visually responsive cells in the MEC (scale bar, 500 mm). Right: average cell density of visually responsive FosTRAP-labeled cells across MEC layers for visual stimulation (dark gray, $n = 6$ mice) compared with control animals (no visual stimulation, light gray, $n = 3$ mice, LMEM with Bonferroni correction, $p < 0.05$).

(C) Example images showing green fluorescent CaMPARI2-labeled cells (first image), photo-converted red fluorescent CaMPARI2-labeled cells (second image), CTip2-positive cells (third image), and merged image (fourth image). Example non-converted cells (white arrowheads), converted Ctip2-positive cells (blue arrowheads), and converted Ctip2-negative cells (purple arrowheads) are indicated.

(D) Proportion of red-converted cells for visual stimulation (R/G, $n = 9$ mice) and control (R/GCtl non-visual stimulation, $n = 2$ mice, LMEM $p < 0.05$) experiments (dark gray).

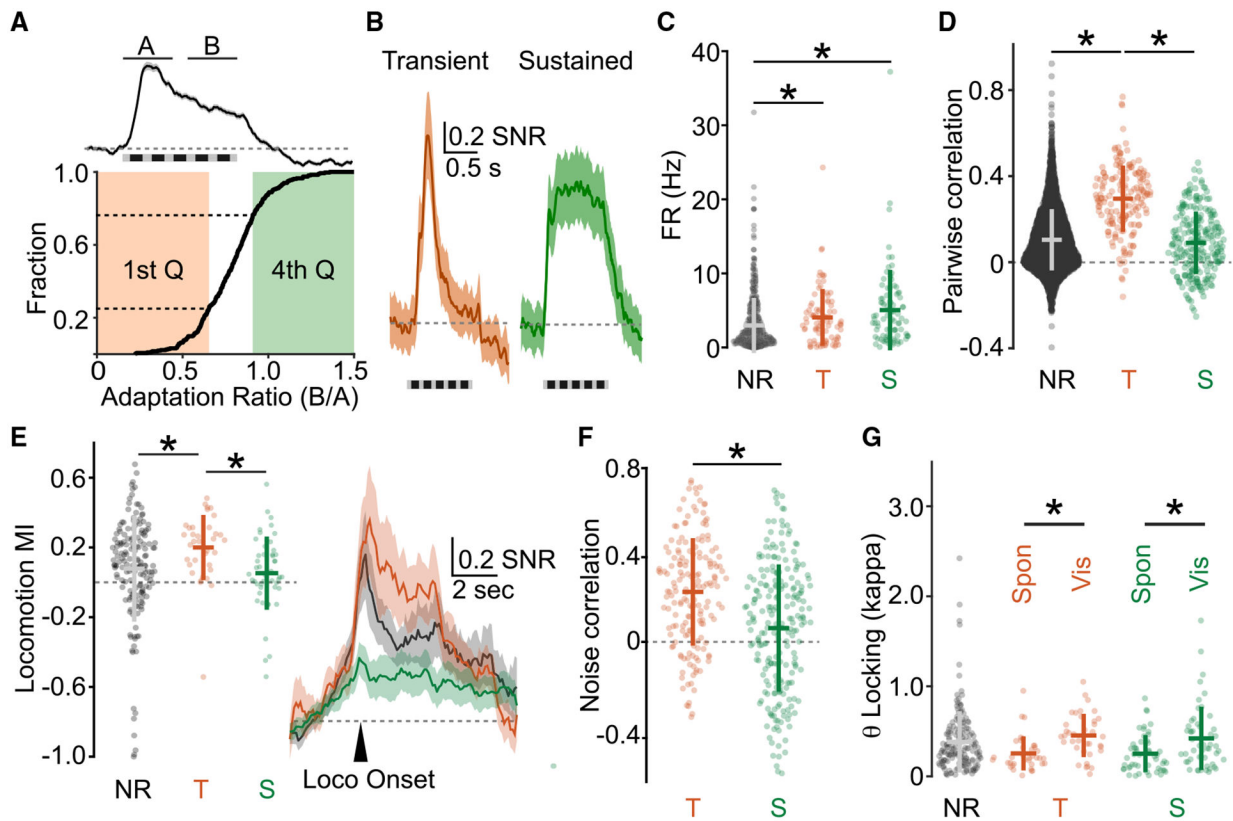Shown is the proportion of red-converted cells expressing Calbindin, reelin, or Ctip2 (light gray).

Unless indicated otherwise, all results are presented as mean ± SD.

Figure 3. Visually responsive MEC neurons exhibit heterogeneous firing dynamics

(A) Cumulative distribution plot of adaptation ratio values (see example at the top) for all visually responsive cells. Lower (orange) and upper (green) quartiles are indicated ($n = 33$ mice, 351 cells).

(B) Average responses across all cells in the lower (transient, $n = 88$ cells) and upper (sustained, $n = 86$ cells) quartiles for adaptation ratio, as in (A) (mean ± SEM). PSTH plots were smoothed with a 50-ms moving window (vertical bar 0.2 SNR, horizontal bar 0.5 s).

(C) Average spontaneous firing rate values for non-responding (gray, $n = 503$ cells in 33 mice), transient (orange, $n = 88$ cells), and sustained cells (green, $n = 86$ cells); LMEM with Bonferroni correction $p < 0.05$.

(D) Average spontaneous pairwise correlation values for the three categories ($n = 503$ non-responsive cells, $n = 88$ transient cells, $n = 86$ sustained cells in 33 mice, LMEM with Bonferroni correction $p < 0.05$).

(E) Left: average locomotion MI for spontaneous activity across cell categories. Right: average firing rate aligned to running onset, smoothed with a 500-ms moving window (mean ± SEM, vertical bar 0.2 SNR, horizontal bar 2 s) ($n = 168$ non-responsive cells, $n = 35$ transient cells, $n = 49$ sustained cells in 14 mice, LMEM with Bonferroni correction $p < 0.05$).

(F) Average noise correlation values for transient versus sustained cells ($n = 503$ non-responsive cells, $n = 88$ transient cells, $n = 86$ sustained cells in 33 mice, LMEM with Bonferroni correction $p < 0.05$).

(G) Average theta-locking values (kappa) during spontaneous and visual stimulation periods ($n = 173$ non-responsive cells, $n = 37$ transient cells, $n = 52$ sustained cells in 15 mice, LMEM $p < 0.05$).

Unless indicated otherwise, all results are presented as mean ± SD.
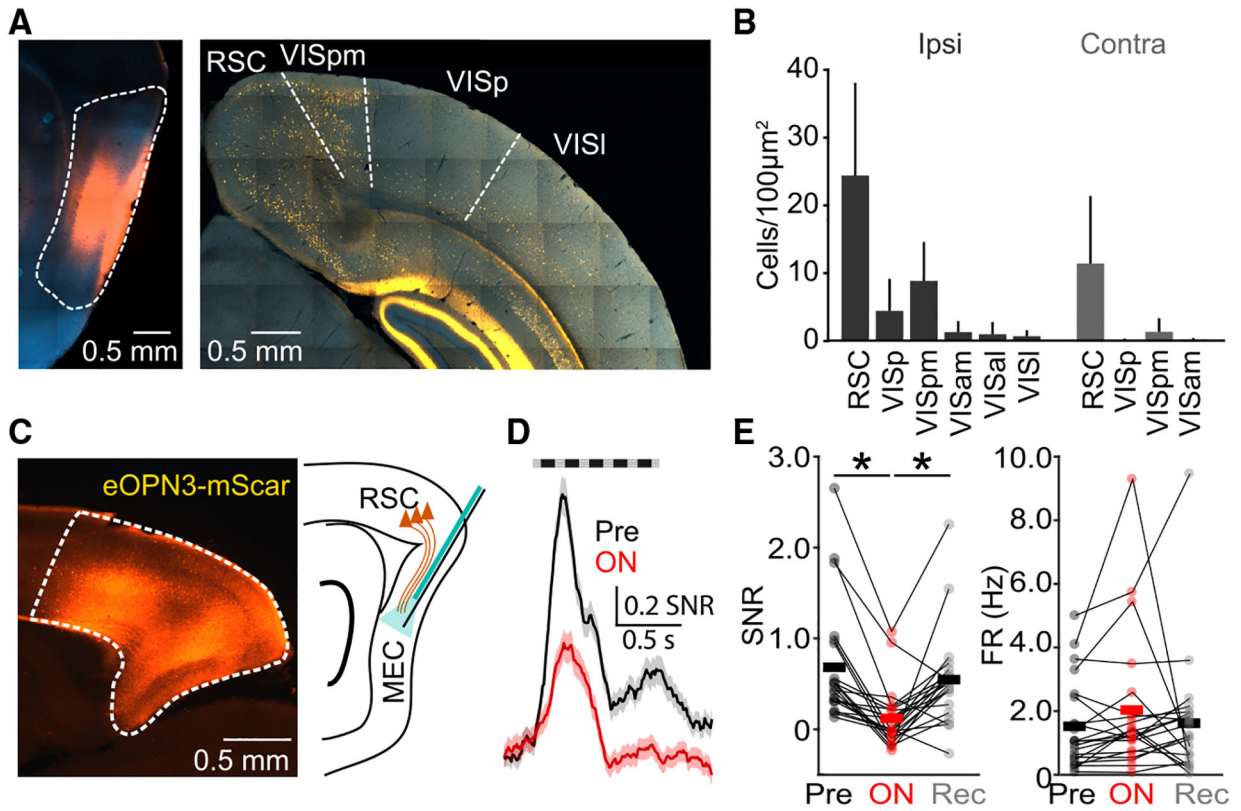
Figure 4. Retrosplenial inputs to MEC mediate visual responses

(A) Left: example image showing expression of the fluorescent CTB-Alexa Fluor-555 label in the dorsal MEC (scale bar, 500 μm). Right: example image of retrogradely labeled cells in ipsilateral neocortical visual areas (scale bar, 500 μm).

(B) Average number of retrogradely labeled cells in the neocortex ipsilateral and contralateral to the MEC injection site ($n = 5$ mice, LMEM with Bonferroni correction $p < 0.05$).

(C) Left: example image showing expression of eOPN3-mScarlet in the RSC (scale bar, 500 μm). Right: schematic representation of MEC RSC termination inhibition.

(D) Average visual responses in MEC neurons before and during optogenetic suppression of RSC afferents (PSTH smoothed with a 100-ms moving window, mean ± SEM, vertical bar 0.2 SNR, horizontal bar 0.5 s), $n = 22$ cells in 4 mice, LMEM with Bonferroni correction $p < 0.05$.

(E) Left: average visual SNR for MEC neurons before, during, and 40 min after optogenetic suppression of RSC afferents ($n = 22$ cells in 4 mice, LMEM with Bonferroni correction $p < 0.05$). Right: average spontaneous firing rate of MEC neurons before, during, and 40 min after optogenetic suppression ($n = 22$ cells in 4 mice, LMEM with Bonferroni correction $p < 0.05$). VISp, primary visual area; VISpm, postero-medial visual area; VISam, antero-medial visual area; VISal, antero-lateral visual area; VISl, lateral visual area.

Unless indicated otherwise, all results are presented as mean ± SD.

KEY RESOURCES TABLE

REAGENT or RESOURCE	SOURCE	IDENTIFIER
Antibodies		
mouse anti-CaMPARI-red	Absolute Antibody	Ab01649-1.1
guinea pig anti-Ctip2	Synaptic Systems	Cat# 325 005; RRID:AB_2620065
rabbit anti-reelin	Invitrogen	Cat# PA5-78413; RRID:AB_2736514
rabbit anti-calbindin	Synaptic Systems	Cat# 214 002; RRID:AB_2068199
goat anti-mouse Alexa Fluor 555	Invitrogen	Cat# A-21422; RRID:AB_141822
goat anti-rabbit Alexa Fluor 647	Invitrogen	Cat# A-21245; RRID:AB_2535813
goat anti-guinea pig-Alex Fluor 647	Invitrogen	Cat# A-21450; RRID:AB_141882
Bacterial and virus strains		
Alexa Fluor 555-conjugated cholera toxin subunit B	Invitrogen	Cat# C34776; RRID:AB_968419
AAV9-CaMKII-Cre	Addgene	Cat# 105551-AAV9; RRID:Addgene_105551
AAV5-hSyn1-SIO-eOPN3-mScarlet-WPRE	Addgene	Cat# 125713-AAV5; RRID:Addgene_125713
AAV1-hSyn-NES-his-CaMPARI2-WPRE-SV40	Addgene	Cat# 101064-AAV1; RRID:Addgene_101064
AAV.hSyn.Cre.WPRE.hGH	Addgene	Cat# 105553-AAV1; RRID:Addgene_105553
Chemicals, peptides, and recombinant proteins		
DiI stain	Invitrogen	D282
Antifade Mounting with DAPI	Vector lab	H-1200-10
Experimental models: organisms/strains		
C57Bl/6 mice	Charles River	C57BL/6NCrl
Ai34D synaptophysin-tdTomato reporter mice	Jackson	Cat# 012570; RRID:IMSR_JAX:012570
FosTRAP mice - Fos-tm2.1-icre-ERT2	Jackson	Cat# 030323; RRID:IMSR_JAX:030323
Software and algorithms		
MATLAB R2021a	MATLAB	https://www.mathworks.com/products/matlab.html
Psychtoolbox	Kleiner et al.[61]	http://psychtoolbox.org/
SHARCQ MATLAB	Kristoffer et al.[62]	https://github.com/wildrootlab/SHARCQ
FMAToolbox MATLAB		https://github.com/michael-zugaro/FMAToolbox
Chronux MATLAB toolbox	Bokil et al.[63]	https://www.mathworks.com/matlabcentral/fileexchange/68537-chronux-analysis-software
CricStat MATLAB tool box		https://www.mathworks.com/matlabcentral/fileexchange/10676-circular-statistics-toolbox-directional-statistics
ImageJ		https://github.com/imagej/ImageJ
CellProfiler	Stirling et al.[64]	https://cellprofiler.org/
FaceMap	Syeda et al.[65]	https://github.com/MouseLand/facemap
Kilosort2	Pachitariu et al.[66]	https://github.com/jamesjun/Kilosort2
Phy2		https://github.com/cortex-lab/phy
Neurosuite	Hazan et al.[67]	http://neurosuite.sourceforge.net